Applied Clay Science 247 (2024) 107200

Contents lists available at ScienceDirect

Applied Clay Science

journal homepage: www.elsevier.com/locate/clay

Bentonite homogenisation and swelling: The effect of salinity

K.A. Daniels [a,*,1], C.C. Graham [a], A.C. Wiseall [a], J.F. Harrington [a], P. Sellin [b]

[a] British Geological Survey, Nicker Hill, Keyworth, Nottinghamshire NG12 5GG, UK
[b] Svensk Karnbranslehantering AB (SKB), Brahegatan 47, Stockholm 10240, Sweden

ARTICLE INFO

Keywords:
Bentonite swelling and homogenisation
Radioactive waste disposal
Saline groundwater
Engineered barrier system
Swelling and porewater pressures
Water uptake

ABSTRACT

Hazardous radioactive waste must be removed from the biosphere, and geological storage is the universally favoured option for accomplishing this. In many cases, the repository designs include a clay buffer as part of the engineered barrier system (EBS) that surrounds the individual waste canisters and seals the disposal galleries. The emplacement of the EBS around the waste will generate small void spaces that must be closed to ensure that high permeability pathways do not develop. Many of the groundwaters at proposed disposal sites are saline, and this porewater chemistry, combined with the presence of technological voids may present a technical challenge to repository designers. In this study, a suite of experiments was conducted to examine the impact of fluid salinity in combination with the presence of a void space on the swelling behaviour of barrier bentonites. Both sodium and calcium bentonites were studied and the sample lengths were varied to provide an understanding of the role of axial strain on the homogenisation and swelling pressure development in the bentonite. After 100 days of testing the clay had swelled into the void space and differential swelling pressures (difference between the maximum and minimum swelling pressure recorded at a given time) had reduced substantially, highlighting the ability of the bentonite to expand into a void. However, clay that swelled into the void never generated significant swelling pressures during the testing period and differential pressures were still significant at the end of the tests. The calcium bentonite demonstrated much smaller peak swelling pressures than the sodium bentonite under the same salinity conditions, and in all tests, the generation of significant swelling pressure in the clay in the low-density end of the sample did not occur during the testing period. These findings suggest that the suppression of clay swelling at higher salinities is likely to strongly impact the void-filling process.

1. Introduction

Disposal of intermediate (ILW) and high (HLW) level radioactive waste and spent nuclear fuel (SNF) in geological repositories is the universally favoured option for removing these hazardous materials from the anthropogenic environment [International Atomic Energy Agency, 2003; Sellin and Leupin, 2013]. Repository designs commonly include canisters to contain the waste sited in deposition holes within a tunnel system that is constructed in a host rock with favourable geological properties [Sellin and Leupin, 2013]. In many cases, the low heat generating wastes (LHGW), of which ILW and low level wastes (LLW) mostly comprise, will be sited in a different part of the repository to the high heat generating wastes (HHGW) [Brady and Kozak, 1995; Stockdale and Bryan, 2013; Daniels et al., 2021b]. For these more radioactive wastes, a clay buffer is often used in the design to surround the space around the individual waste canisters [Sellin and Leupin, 2013]; this is known as the engineered barrier system (EBS). The same material used as a backfill can also seal the disposal galleries from access to the surface.

Bentonite is the favoured material for use as the EBS and backfill in many radioactive waste repository designs [Sellin and Leupin, 2013; Pusch, 1977]. A detailed knowledge of this EBS behaviour over a timescale of around 1 million years is required to demonstrate that a geological repository will be able to safely contain HHGWs [Sellin and Leupin, 2013]. The EBS will occupy the void space around the waste canisters and must be able to both prevent migration of fluids and ensure canister stability and self-sealing/healing [SKB, 2007; Komine, 2010; Svoboda, 2013; Chen et al., 2018]. Bentonite is smectite rich and as such, has a high swelling capacity [Villar and Lloret, 2008; Wang et al., 2013; Bian et al., 2018; Harrington et al., 2020; Zeng et al., 2020; Watanabe and Yokoyama, 2021]. The exact repository design and barriers used will depend on the available geology and appropriate depth of

* Corresponding author.
E-mail address: DanielsK4@cardiff.ac.uk (K.A. Daniels).
[1] Present address: School of Earth and Environmental Science, Cardiff University, Main Building, Park Place, Cardiff, CF10 3AT, U.K.

https://doi.org/10.1016/j.clay.2023.107200
Received 30 January 2023; Received in revised form 26 October 2023; Accepted 1 November 2023
Available online 17 November 2023

construction, as well as the waste inventory requiring disposal [Sellin and Leupin, 2013; Chapman, 2006; Delage et al., 2010; Chapman and Hooper, 2012]. Regardless of the host rock under consideration, repository concepts often incorporate the EBS as blocks that are placed around the waste canister [Wang et al., 2013; Liu, 2010; Andra, 2005; Martin et al., 2006; Juvankoski, 2010], necessarily generating small void spaces that will need to be closed to ensure high permeability pathways do not exist within the EBS [Börgesson and Pusch, 1987; Wang et al., 2013; Jia et al., 2019; Harrington et al., 2020; Daniels et al., 2021b].

A number of different bentonites have been considered for use within European repositories [SKB, 1983; NAGRA, 1985; Coulon et al., 1987; Linares, 1989; Vieno et al., 1992; Pusch, 2001; Villar, 2002; Tabak et al., 2007; Sun et al., 2017; Villar et al., 2020], although the focus has been placed more heavily on the sodium (Na) bentonites [Cui, 2017] such as the Wyoming-type MX80 [Pusch, 2001], GMZ bentonite [Ye et al., 2009], and Turkish Resadiye [Tabak et al., 2007]. Calcium (Ca) bentonites (e.g. [Daniels et al., 2021a]) (such as the Fourges Clay and the Černý Vrch deposit) have also received attention however, due to their naturally good availability for certain nations [Börgesson and Pusch, 1987; Sun et al., 2017; Coulon, 1987; Tessier et al., 1998; Marcial et al., 2002]. Comparative studies between the two types of bentonite have indicated that the water soption is higher for smectites composed of cations with a higher ionic potential of the exchangeable cation and larger hydration energy [Dontsova et al., 2004; Villar, 2007]. Ca bentonites have a greater retention capacity than Na bentonites [Hall and Astill, 1989; Caballero et al., 2004], although for very strongly compacted bentonites and high relative humidities (RH = 99.9%) at suctions below 0.1 MPa, Na bentonites can sorb more water [Villar, 2007]. Marcial et al. [2002] found that Ca bentonites have slightly higher void ratios for a given dry density due to the larger size of the divalent Ca^{2+} cation.

The rate of swelling of the bentonite in an EBS will dictate how quickly the material can isolate the radioactive waste from the surrounding environment, and is dependent on the bentonite dry density, fluid availability and composition, the pore pressure magnitude and the waste temperature [Daniels et al., 2021b; Harrington et al., 2020]. Where sufficient voidage exists to enable swelling strain to occur, the bentonite dry density will decrease, affecting the hydromechanical properties of the EBS [Daniels et al., 2021b; Komine, 2010; Bian et al., 2018; Harrington et al., 2020; Komine et al., 2009; Dueck et al., 2016; Dueck et al., 2019]. Anisotropy in the hydromechanical properties due to non-uniform swelling presents a significant challenge to the repository safety case, should the material heterogeneities persist in the long-term [Daniels et al., 2021b; Harrington et al., 2020; Brackley, 1973; Imbert and Villar, 2006; Gens et al., 2011; Harrington and Tamayo-Mas, 2016; Massat et al., 2016; Harrington et al., 2017]. Important material parameters including the swelling pressure, permeability, strength and friction coefficients will therefore all be affected by the time-dependent development of porewater pressure [Harrington et al., 2017], potentially leading to strongly-localised material heterogeneity; this has been observed in both laboratory and full scale experiments [Villar et al., 2020; Wigger et al., 2017].

The porewater chemistry also plays an important role on the mechanical behaviour and development of swelling pressure in the EBS [Di Maio, 1996; Karnland et al., 2005; Castellanos et al., 2008; Herbert et al., 2008; Siddiqua et al., 2011; Zhu et al., 2013; Zhang et al., 2019; Chen et al., 2022]. Previous studies showed that as the salinity of the groundwater increased, the permeability increased and the swelling pressure decreased [Komine et al., 2009; Karnland et al., 2005; Castellanos et al., 2008; Herbert et al., 2008; Zhu et al., 2013; Studds et al., 1998; Mata, 2003; Villar, 2005; Karnland et al., 2006; Sun et al., 2015]. Naturally occurring saline groundwaters are distributed worldwide and salinisation problems are contributing to an increase in their prevalence [Li et al., 2020]. The groundwaters encountered at the Bruce Nuclear Site in Ontario, Canada (3.8 M NaCl [Ltd., 2011; Daniels et al., 2017]), which is proposed to host a Deep Geological Repository (DGR) for ILW and Low Level Wastes (LLW), are an extreme case; however, within Europe, the groundwaters in areas under consideration for the development of final geological repositories can still be fairly saline (e.g. the Olkiluoto groundwater with an NaCl-dominated composition, an ionic strength of approximately 0.2 M and approximately 10 g/L of total dissolved solids [Hella et al., 2010; Wersin et al., 2016]). Much effort has been made to understand the role of porewater chemistry and salinity on the behaviour of bentonite barriers [Chen et al., 2018; Karnland et al., 2005; Herbert et al., 2008; Zhang et al., 2019; Chen et al., 2022; Sun et al., 2015; Li et al., 2020; Karnland, 1997; Karnland and Muurinen, 2002; Bradbury and Baeyens, 2003; Chen and Huang, 2013; Chun-Ming et al., 2013; Liu, 2013; Wang et al., 2014; Chen et al., 2015; Chen et al., 2016; He et al., 2016; Navarro et al., 2017b, 2017a], as well as the role of engineering voids on the barrier performance [Daniels et al., 2021b; Wang et al., 2013; Bian et al., 2018; Harrington et al., 2020; Zeng et al., 2020; Watanabe and Yokoyama, 2021]. However, the combination of the presence of engineering voids and a saline groundwater has not been addressed. The main objective of this test programme was to investigate the impact of fluid salinity on the swelling behaviour of bentonite in the prescence of a void. Samples of varying length were used to examine the influence of permitted axial strain on homogenisation and swelling pressure development in both Na and Ca bentonites. The experiments presented in this study build upon the work of Harrington et al. [2020] and Daniels et al. [2021b] who investigated bentonite homogenisation and swelling pressure development under zero-salinity conditions and at ambient and elevated temperatures respectively.

2. Experimental materials and method

2.1. Sample preparation

The engineered clay samples used for testing were composed of either a Wyoming-type Na bentonite (MX80; Tests 1–3 and 5) or a Korean Ca bentonite (Test 4). The Na bentonite powder was supplied by the American Colloid Company (now Mineral Technologies Inc. (New York, NY, USA)) through Sibelco Nordic, who also dried the material and crushed it to a granular powder with an average particle size ranging from 16 to 200 μm [Svensson et al., 2017]. The Wyoming-type bentonite MX80 is used in the Engineered Barrier System (EBS) design for the Swedish disposal facility [SKB, 2011; Idiart and Pekala, 2016; Svemar et al., 2016]. The sodium Wyoming-type MX80 bentonite mineralogy was obtained from XRD of a subsample of the raw powder conducted at the British Geological Survey (BGS): montmorillonite (91.7%), plagioclase (2.7%), K-feldspar (1.7%), quartz (2.7%), cristoballite (<0.5%), calcite (<0.5%), gypsum (<0.5%), pyrite (<0.5%). The cation exchange capacity (CEC) of the batch of MX80 supplied to the BGS was 75 (meq/100 g), and the exchangable cations were as follows: Na- 75%; Ca- 16%; Mg- 7%; K- 2% [SKB, 2011].

The Korean calcium bentonite (KJ-II) was supplied as a fine powder (<250 μm) with a moisture content of ~11–12% by the Korean Atomic Energy Research Institute (KAERI); this bentonite is considered for use as the EBS in the Korean programme. The Korean bentonite mineralogy was measured by KAERI and the data supplied to the BGS with the powder as follows: montmorillonite (smectite; 61.9%), albite (20.9%), quartz (5.3%), cristoballite (4.1%), calcite (4.8%), heulandite (3.0%). The cation exchange capacity (CEC) was 84 (meq/100 g), and the exchangable cations were as follows: Ca- 63%; Mg- 26%; Na- 9%; K- 2% [Goo et al., 2023].

All of the bentonite samples were compacted at the BGS from the Na or Ca bentonite powders. The powder was mixed with a known quantity of deionised water and compacted in a cylindrical steel pressure vessel at 80 MPa axial pressure (with constant radial confinement) for 24 h to produce a test sample at 100% saturation. Lead shot was placed into the clay powder in a cross shape at two discrete levels (21 pieces per level)

whilst the sample was being prepared and compacted. This allowed swelling in the sample interior and frictional processes during compaction to be investigated using X-Ray Computed Tomography (XCT). Five pieces of lead shot were also pushed into the top face of the sample immediately prior to compaction to aid with sample orientation and thus indicate the way up of the sample. When the sample was prepared for installation into the testing apparatus, care was taken to maintain the line of lead shot in the one sample face so that the pre- and post-test XCT images could be cross correlated. The sample compaction direction during manufacturing aligned with the long axis of the experimental apparatus and expansion direction in all test cases. The samples produced had a target dry density of 1.7 g/cm^3; this was confirmed by weighing and drying a sample that was specifically prepared to obtain the post-compaction dry density and to make sure that the subsequent samples produced would all share the same geotechnical parameters. This procedure was followed for both the Na- and Ca-bentonite. The first Na-bentonite sample prepared had a measured dry density of 1.702 g/cm^3 and all of the following samples were then made in the same way. The basic geotechnical properties of the test samples are shown in Table 1. Despite the intention to vary the permeant salinity in this suite of tests, the sample preparation fluid was chosen to be deionised water to ensure that the samples tested with saline groundwaters in this study would be the same as those previously tested at ambient [Harrington et al., 2020] and elevated temperatures [Daniels et al., 2021b].

Each test sample was manufactured with a diameter to push-fit into the interior diameter of the apparatus; the sample length was manufactured to a specific starting length requirement for each test (Table 1). To achieve the correct starting dimensions and ensure the sample would precisely fit the interior of the pressure vessel used during testing, the sample was turned down in a machine lathe, whilst also preserving the orienting lead shot in the top face. The lathing was completed without water to prevent any sample swelling prior to testing. To minimise sample moisture loss during preparation, the sample was wrapped in plastic film whenever possible, and immediately vacuum sealed and bagged once the lathing process was complete. Once lathed to the correct dimensions, the sample was scanned in the Geotek Rotating XCT scanner in the British Geological Survey's Core Scanning Facility. During XCT scanning the image was split into a number of scan slices. Each scan slice had a defined thickness that was dependent on scan resolution. Using this scan slice thickness, it was possible to assign to each lead layer a scan slice number and calculate the number of scan slices between each end of the sample and the lead layers, as well as the number of slices between the two lead layers, enabling comparison between the pre- and post-test scan data. The sample's starting dimensions and mass were measured immediately before each test commenced.

2.2. Experimental method

The experimental apparatus used for the swelling tests had a constant volume configuration, with an internal length of 116 mm and a diameter of 60 mm. The sample was constrained in a radial direction, but the apparatus allowed axial swelling. This was a bespoke set-up that was designed and built at the BGS (Fig. 1) and consisted of (1) a thick-walled, dual-closure pressure vessel; (2) an injection pressure system; (3) a backpressure system; (4) 5 bespoke pressure transducers measuring radial and axial total stress; (5) 12 radial pore pressure transducers to monitor local evolution along around the sample; and (6) a microcomputer-based high-speed data acquisition system. The pressure vessel was comprised of a dual-closure tubular vessel manufactured from 316-stainless steel, pressure-rated to 70 MPa, with the internal surfaces hard-chromed to prevent damage. Large axial sintered filters were also recessed into the end closures to ensure an even distribution of fluid entering the vessel at each of its ends. The axial pushrods connected to the axial load cells protruded through the sintered filters to be able to touch the surface of the clay. The test fluid was supplied to the sample using high precision syringe pumps (Teledyne ISCO D-Series 260D). In these experiments the pressures stayed within the range of 0–10 MPa, however, the pumps were capable of reaching pressures of up to 65.5 MPa, while maintaining excellent low-flow stability. Each pump piston was controlled by a microprocessor that continually monitored an optically encoded disc with 16.63 nL graduated segments, and adjusted its rotation rate using a DC-motor and geared worm drive. The pumps could therefore be operated in constant pressure or continuous flow modes, with a flow rate accuracy of ±0.5%. The pumps were factory calibrated for volumetric control, and as laboratory calibration of the volumetric control was not possible, the tests were designed to minimise pump error.

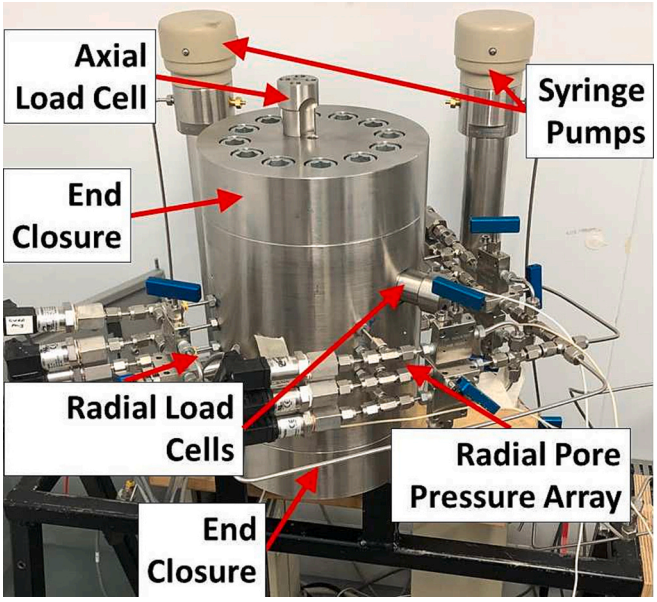

Fig. 1. The test apparatus showing the locations of the porewater pressure transducers and load cell housings.

Table 1
Starting sample dimensions and void length, bentonite type, pre-test geotechnical parameters, permeant salinity and test duration. In all tests an ambient temperature of 20±1 °C was maintained, the pore pressure was held at a constant 4500 kPa and the starting sample dry density was 1.702 g/cm^3 for the Na bentonites and 1.7 g/cm^3 for the Ca bentonite.

Test Number	Sample Identifier	Bentonite Type	Sample Length (mm)	Sample Diameter (mm)	Sample Mass (g)	Bulk Density (g/cm^3)	Void Length (mm)	Permeant Salinity (M NaCl)	Test Duration (days)
1	FPR-20-001	Na bentonite	65.30	59.84	381.56	2.078	50.70	1	119.9
2	FPR-20-026	Na bentonite	75.43	59.92	439.95	2.068	40.57	1	99.7
3	FPR-20-018	Na bentonite	85.00	59.49	494.20	2.091	31.00	1	100.2
4	FPR-20-011	Ca bentonite	65.16	58.68	364.55	2.068	50.84	1	98.5
5	FPR-21-023	Na bentonite	65.27	59.66	380.81	2.087	50.73	3	100.1

This apparatus was instrumented with 5 load cells (2 axial and 3 radial) and 3 transducer arrays to measure the total stress and pore pressure respectively. The pore pressure measurement ports were fitted with porous plugs to prevent clay material from migrating up the instrumentation holes. The load cells in this apparatus were button-type XF2041–3-2kN temperature-compensated load cells, with a range of 0–25 MPa supplied by StrainSense Ltd. The load cells were positioned on the outside of the pressure vessel and held in stainless steel housings, preventing any direct interaction between the sensor and the test permeant. The force was translated from the clay to the load cells via tungsten carbide pushrods, chosen for their hardness and incompressibility. This configuration allowed the swelling stress of the clay to be translated to the load cell, but due to the indirect nature of the measurement, meant that the data were slightly more prone to hysteresis due to the frictional effect of the o-ring seals along the pushrod axis. The load cell measurements can be considered as accurate to ±80 kPa, whilst the pore pressures should be considered accurate to ±15 kPa. Ambient temperature conditions were maintained throughout testing; testing was conducted inside an air-conditioned environmental chamber, which maintained conditions at 20 °C ∼ ±1 °C. A schematic diagram showing the positions of each of the points of measurement on the testing apparatus is provided in the supplementary material (Figure SM1). The supplementary material is available online.

At the start of each experiment in the testing programme, the apparatus was calibrated. The calibration was carried out by placing a steel bung in the bore of the test vessel and filling the apparatus with the test fluid (1 or 3 M NaCl). All of the tubework was carefully flushed with the test fluid through each available port to ensure no residual air remained. A constant water pressure was then applied by one of the syringe pumps in 1 MPa increments from 1 to 7 MPa and back to 1 MPa. At each pressure increment, the pressure was held constant and the response on each of the sensors and on a Druck pressure calibration instrument was measured. This data was then used to provide a calibrated pressure output for each sensor. After calibration, the steel bung was removed from the vessel and the tubework was carefully flushed again. After flushing, the sample was immediately installed to prevent any air ingress into the tubework connecting the sample to the pore pressure sensors. The sample was pushed to the base of the void inside the apparatus and the remaining void space above the sample was immedaitely filled with the test fluid. The same fluid was also used as the external pressurising fluid.

Testing was carried out at an applied water pressure of 4500 kPa, which was selected as a suitable reference value for comparison with the Swedish radioactive waste repository concept, as outlined by SKB [Rhén et al., 1997; Svemar et al., 2016]. To start the test and reach the target water pressure whilst keeping the sample fixed in position, the pressure was applied alternately to each end of the sample in incremental steps, starting at the end of the apparatus that was originally void space. The pressure within the original void space was always higher than that at the base of the apparatus until both ends reached 4500 kPa. This process only took a few minutes, but occurred as soon as the sample had been installed and prevented the sample from sliding along the bore of the vessel before the sample swelling began.

The flow rate into and/or out of the sample was controlled and monitored using the syringe pumps and a single digital control unit. Each pump was operated in a constant pressure mode and thus the flow rate and direction were not prescribed. Inflow or outflow could therefore occur at either end of the test vessel. Once the pore pressure had been applied to the sample, no further external hydraulic gradient was applied to the clay. FieldPoint^{TM} and cRIO logging hardware and the LabVIEW^{TM} data acquisition software (National Instruments Corporation, Austin, TX, USA) were used to log the test at 2 min intervals and provided a detailed time series dataset; the parameters logged were flow rate, total stress and pore pressure. Over the duration of each test, the sample was able to swell in an axial direction into the remaining interior void space, until the clay filled the full length of the pressure vessel. Upon completion of testing, the criterion for which was that the total stress measured on each sensor had approached an asymptote and usually occurred within 100 days, the samples were carefully extruded whole from the vessel using a hydraulic ram, immediately wrapped in clingfilm and sealed in plastic using a vacuum sealer to minimise moisture loss, before being XCT scanned. After XCT scanning, the post-test sample was cut into approximately 10 mm thick slices. These slices were weighed, placed in an oven at 105 °C and dried for 24 h to determine the moisture content (the difference between the pre-test wet and post-test dry weights as a fraction of the post-test dry weight).

3. Results

To examine the influence of salinity on the swelling pressure of bentonite in the presence of a void, a series of 5 experiments were conducted using an NaCl solution to enable saturation and swelling of the clay. The test parameters and starting conditions are given in Table 1. In the first 24 h of Test 1, a water pressure of 5 MPa was erroneously applied to the sample, and this may have affected the swelling pressures measured in Test 1 over the first couple of days, particularly the peak swelling pressure which occurred around this time. Also for Test 5 (3 M NaCl), as a result of its low bulk density, low strength and liquid consistency particularly at the end of the apparatus that was void space at the start of the test, it was not possible to retrieve subsamples of the post-test clay. It should also be noted that there were number of sensor failures in these experiments, meaning that data could not be collected at every sensor location in every test.

3.1. Development of swelling pressure

Swelling pressure was calculated as the difference between the measured total stress (on the axial and radial sensors) and the average applied water pressure (between the two pumps). The resulting swelling pressure distributions for the two axial sensors, and the radial sensor closest to the base of the vessel are shown in Fig. 2, and the curves for all sensors and all tests (Tests 1 to 5) are given in Figure SM3 in the supplementary material. The development of pressure was spatially complicated and significant variance still existed after 100 days of testing. The swelling pressures generated over the first 10–15 days of testing were seen to vary substantially at different measurement locations in each of the tests. The lowest swelling pressures were recorded at the void end of the vessel and the highest swelling pressures were detected at the end where the clay sample was initially present (Table 2). Higher stress values were seen to reduce with time, resulting in a degree of convergence. However, lower swelling pressures were not seen to increase significantly during the course of testing and remained at or below zero throughout the duration of the test. On some sensors, the measured values of total stress did not exceed the magnitude of the average applied water pressure, resulting in the calculation of negative values.

For Tests 1, 2 and 3, which had varying starting lengths but otherwise had the same experimental parameters (Na bentonite, 1 M NaCl test permeant), higher end-of-test swelling pressures were observed for longer initial sample lengths, as was expected. However a greater swelling pressure difference between the largest and smallest measured stresses at the end of the test period also existed for the longer initial sample length. The largest end-of-test swelling pressure difference was seen in Test 3 (85 mm) between the A1 (axial top) and R1 (radial base) sensors. In general, a significant heterogeneity in the observed stress distribution persisted in the 1 M NaCl tests, even after 100 days. When the exceptionally high concentration pore fluid of 3 M NaCl was used (Test 5), minimal swelling pressure was detected over the 100 day period. Graphs of the swelling pressure development for each of the tests are given in the supplementary material (Figure SM3). This observation was in line with the expected inhibition of swelling under these

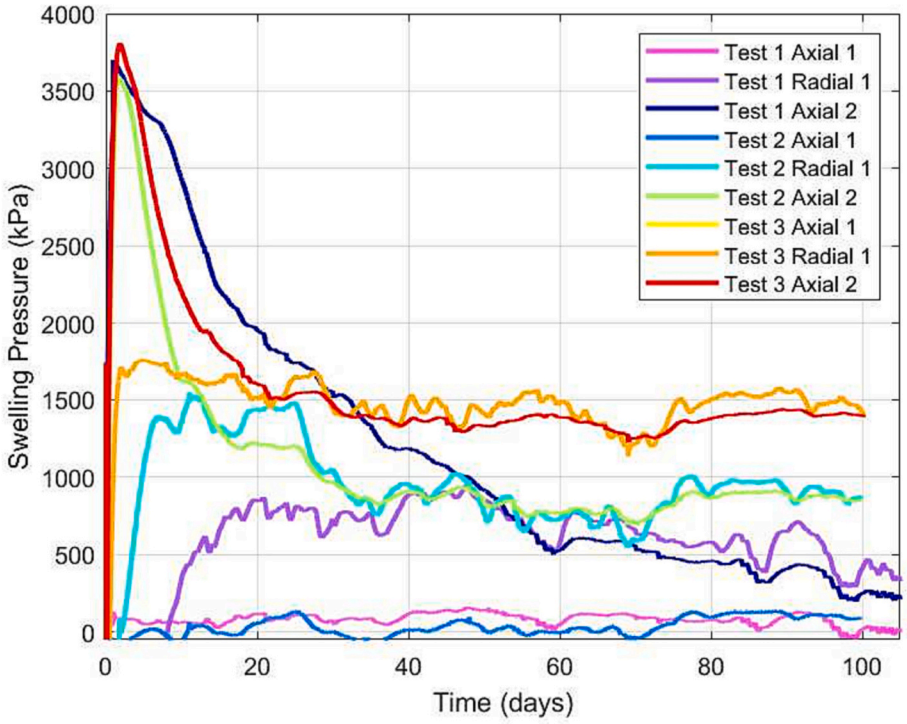

Fig. 2. Swelling pressure evolution for high salinity swelling Tests 1, 2 and 3. Each of these tests used a 1 M NaCl solution as the test permeant and each was conducted using Na bentonite. The starting sample lengths were 65, 75, and 85 mm for Tests 1, 2, and 3 respectively. Data from the two axial and one radial (Radial 1; closest to the base of the vessel) sensor are presented to allow better visual comparison between the tests. Sensor locations can be found in the schematic diagram (Figure SM1) in the supplementary material. The data for Test 3 Axial A1 do not appear on the graph because at all times the apparent swelling pressure was below zero.

Table 2
The peak and averaged end-of-test swelling pressures measured during each test. The largest peak axial swelling pressures were always observed on the sensor at the base of the vessel. The sensor that the largest peak radial swelling pressure value occurred on was always R1 (also closest to the base of the vessel). The average swelling pressures and 'Axial base' are calculated from the end-of-test values over approximately the final 6 h of data. [a]The test was allowed to run to 119.9 days, so the swelling pressure data is given for the 6 h leading up to day 100 to be comparative with the other test datasets. [b]The sensor R2 was logging a thermocouple channel and sensor R3 had developed a fault, so for Test 3 only sensor R1 was available. [c]Sensor R3 had developed a fault so only sensors R1 and R2 were used to calculate the average radial swelling pressures for Test 4.

Test Number	Peak Axial (kPa)	Peak Radial (kPa)	Average Axial (kPa)	Average Radial (kPa)	Axial Base (kPa)
1[a]	3702	949	114	159	234
2	3594	1546	469	526	851
3[b]	3811	1771	619	1432	1396
4[c]	2083	336	−38	−289	99
5	−139	515	−144	−256	–

conditions and was backed up by observations during decommissioning, at which time the clay at the low density end of the test cell was found to be in a fluid state (Fig. 3).

3.2. Development of pore pressure

A marked difference was apparent in the pore pressure equilibration time between experiments (Fig. 4 and Figures SM4 to SM9 in the supplementary material). The shorter the initial sample and the greater the degree of axial swelling permitted, the more rapidly pore pressures were able to equilibrate along the length of the sample. This observation was consistent with the expected reduction in dry density, as a result of sample swelling, which caused an increase in permeability and a more rapid redistribution of water within the clay. Comparison of pore pressure evolution between Tests 1, 4 and 5, in which the same degree of axial swelling was permitted (Fig. 4), showed that the higher salinity of 3 M NaCl led to a substantially faster approach to hydraulic equilibrium than the 1 M NaCl test for the same bentonite composition. In addition, the Ca bentonite (Test 4) showed a much faster approach to hydraulic equilibrium than the Na bentonite for otherwise the same conditions. Whilst it took more than 20 days for all of the pore pressure transducers in Test 1 to reach the applied pore pressure, in Test 4 this took less than half of this time. The pore pressure data from Test 4 suggest that Ca bentonites will swell more quickly than Na bentonite in a higher salinity environment.

3.3. X-Ray CT sample imaging

Pre- and post-test X-Ray Computed Tomography (XCT) was used as a diagnostic tool to examine the swelling of the interior of the sample and to provide knowledge about the role of frictional effects along the side wall of the test vessel. The compacted pre-test samples were initially scanned, then once each test had finished and prior to the post-test geotechnical measurements being carried out, the sample was re-scanned (with the exception of the Test 5 post-test sample, which was too liquid). This facilitated both qualitative and quantitative image analysis to aid further investigation of the internal sample swelling. The volume change of the sample as a result of swelling during the testing period was qualitatively shown by the XCT data through the difference in sample size pre- and post-test (Fig. 5; Test 2: 75 mm, 1 M NaCl sample).

In the pre-test scans of the samples, a degree of concavity was noted in the lead shot layers, with the lead shot at the sides positioned higher than the lead shot in the centre of the compacted sample. This was

Fig. 3. During decommissioning of Test 5 (3 M NaCl), the clay was found to be in a fluid state at the end of the vessel which originally contained only water.

attributed to frictional effects during the initial compaction of the samples, which allowed slightly greater vertical movement through the centre of the sample than was possible at the sample edges. In Tests 1 and 3, the sample was installed into the vessel with these pieces of lead shot on the top face, adjacent to the void space. In Test 2 the sample was installed with these pieces of lead shot on the bottom face, at the base of the testing vessel. After the testing period the concavity in Test 2 (Fig. 5) could be seen to have slightly increased, indicating that friction on the side walls may have played a minor role in slowing the sample expansion at the edges. Such frictional effects are a necessary complication of real-world experimentation and will also occur in the environment of the Geological Disposal Facility, for which end-use these materials are being considered.

Nevertheless, these observations do also demonstrate that lead shot within the centre of the clay was displaced substantially during testing, as a result of the swelling process (Fig. 5). During XCT scanning the image was split into a number of scan slices. Each scan slice had a defined thickness that was dependent on scan resolution. Using this scan slice thickness, it was possible to assign to each lead layer a scan slice number, and calculate the number of scan slices between each end of the sample and the lead layers, as well as the number of slices between the two lead layers. Comparison with the pre- and post-test scan data therefore allowed a degree of swelling in each section of the sample to be defined (Fig. 5). Please see the supplementary material for additional methodological information.

In all tests, the greatest section thickness change occurred in the ends of the samples closest to the void space at the start of the tests (Fig. 5). Test 3 (with the longest pre-test length) saw less overall swelling along the total sample length, and the swelling was mainly concentrated at the top end (void space at the start of the test). In Tests 1 and 2, a higher degree of swelling occurred down the entire length of the sample. Unfortunately, the uppermost section of the shortest sample (Test 1; 65 mm start length) had disintegrated during the post-test dismantling of the test apparatus, and therefore a data point was missing. This also impacted the post-test moisture content measurement.

3.4. *Post-test moisture content and dry density*

Measurements of the moisture content were made after depressurisation of the apparatus, removal of the test samples and post-test XCT scanning. Despite each sample swelling to completely fill the apparatus' internal volume, there was an extreme difference in the consistency of the samples along their length. In the 3 M NaCl case in particular (Test 5), the top of the sample was essentially liquid. The moisture content was used to provide information about the spatial variability in sample properties, homogenisation and to help interpret the observed swelling response. Upon removal from the test vessel, the sample was vacuum sealed then XCT scanned; each post-test sample was subsequently subsampled along its length using a sharp knife to slice the sample and a bespoke steel sample holder with a 2 mm screw thread lead to enable the subsampling to be well controlled in the axial direction. Each slice was weighed before being dried at 105 °C for at least 24 h. The experiments were carried out during 2020 and 2021; due to restrictions resulting from the global Coronavirus Disease 2019 (COVID-19) pandemic, it was not possible for every post-test sample to be dried for exactly 24 h. The

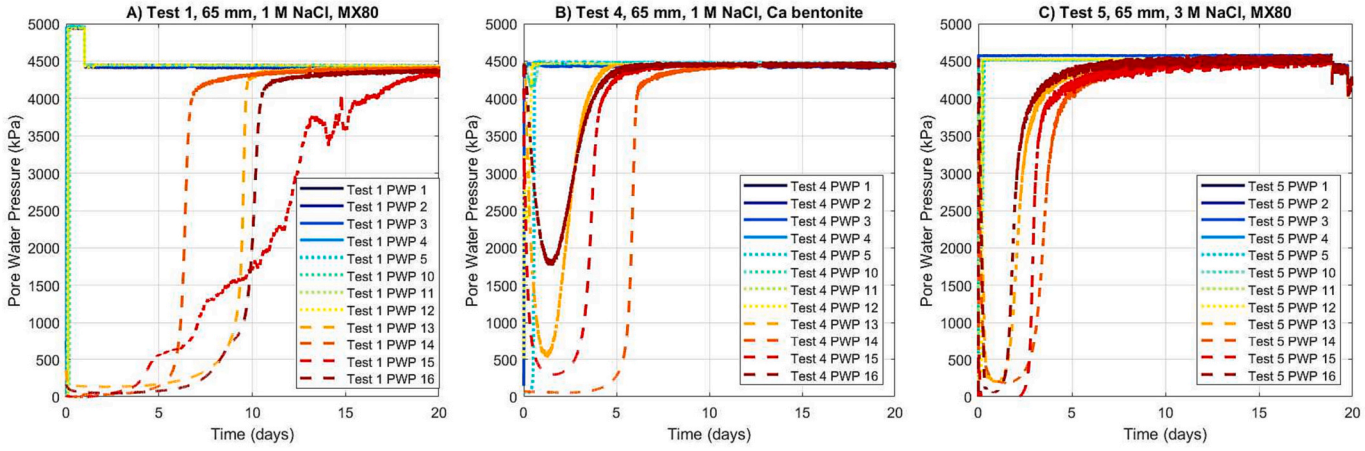

Fig. 4. Pore pressure evolution for the three high salinity swelling experiments that had a 65 mm starting sample length (Tests 1, 4 and 5). A 1 M NaCl solution was used for Tests 1 and 4, whilst a 3 M NaCl solution was used for Test 5. Tests 1 and 5 used Na bentonite, whilst the Test 4 sample was compacted from a Ca bentonite powder. The location of each of the porewater pressure arrays can be found in the schematic diagram (Figure SM1) in the supplementary material.

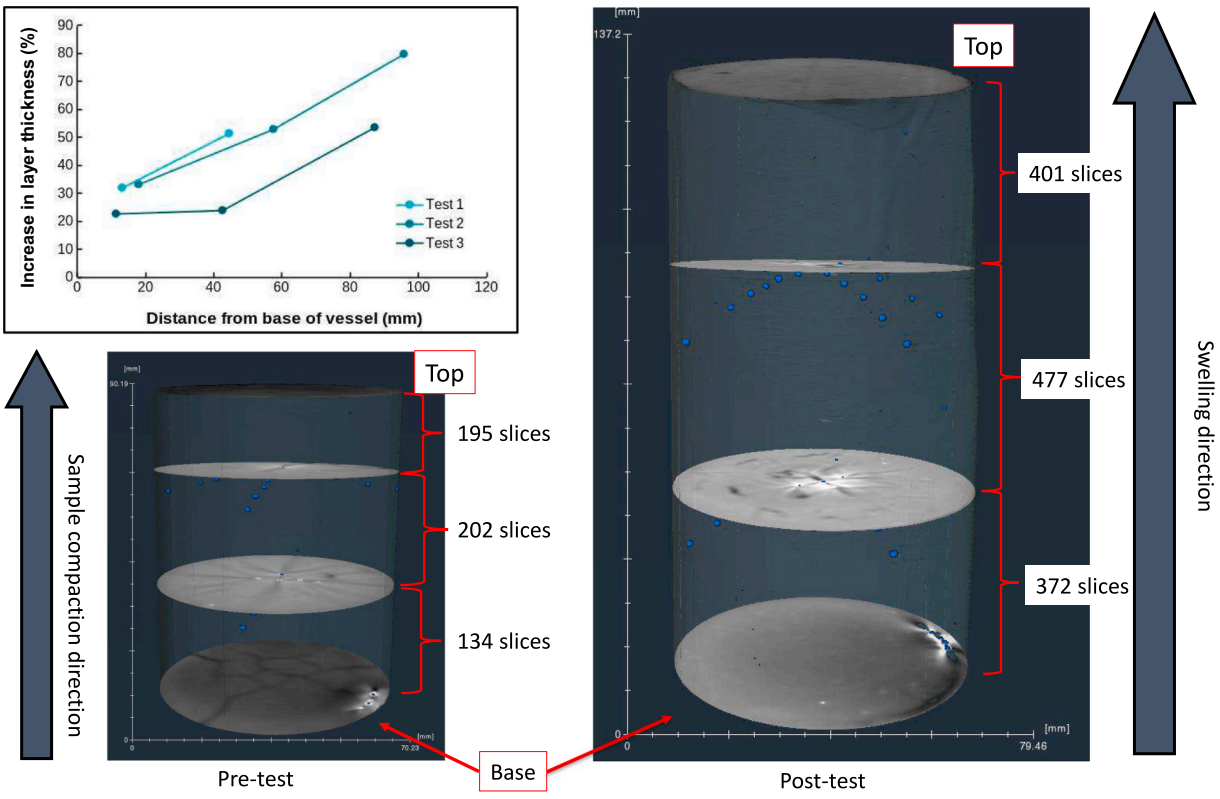

Fig. 5. CT images showing lead shot distribution for Test 2 (L_0=75 mm, 1 M NaCl) before (left) and after (right) testing; and a plot of the percentage increase in thickness of sections of the sample, as a function of the distance from the base of the vessel to the midpoint of that section for the three Wyoming-type Na bentonite tests run using 1 M NaCl test permeant (Tests 1, 2 and 3). These sections were defined as the clay between the lead layers, and the clay between each end of the sample and the nearest lead layer. The line of 5 pieces of lead shot at the edge of the sample used for orientation purposes was placed into the upper surface of the sample immediately before compaction and indicated the way up of the sample.

Test 1 sample was in the drying oven for significantly longer, and this should be considered when interpreting the moisture content and dry density data. Following the method in Whitlow [2004], the post-test weight gave the mass of solid material, and the difference between the pre- and post-test weights gave the mass of water within the sample; from these values the moisture content was calculated. The post-test dry density values were calculated from the moisture content assuming a specific gravity of 2.77, a saturation of 1 and using the density of water (corrected for salinity). The degree of saturation S was assumed to be equal to 1 because the degree of saturation of each pre-test sample was close to unity and the void was filled with saline water.

The resulting moisture content and dry density profiles further demonstrated the influence of salinity and axial strain on the resulting geotechnical properties of the clay after swelling (Fig. 6). Interestingly, the moisture content profiles for Tests 1 and 4 (both 65 mm tests with 1 M NaCl, but with different bentonite compositions) mapped closely on top of one another, except for the top measurement in Test 4, which had a much higher moisture content. Moisture contents from the uppermost 20 mm of the sample in Test 1 were not available; the fluidity of the sample in the upper portion of the post-test sample was unexpected. In Test 1 therefore, the upper portion of the sample was able to escape from the vessel as the end closure was removed. The moisture contents (and corresponding dry densities) for Test 5 (3 M NaCl) could not be obtained, because the clay was fluid at the low density end after testing. Each sample showed a marked increase in the moisture content at all points of measurement, although there was a larger increase at the upper end of the sample that was void space at the start of the test. A relationship between the sample length and moisture content increase was

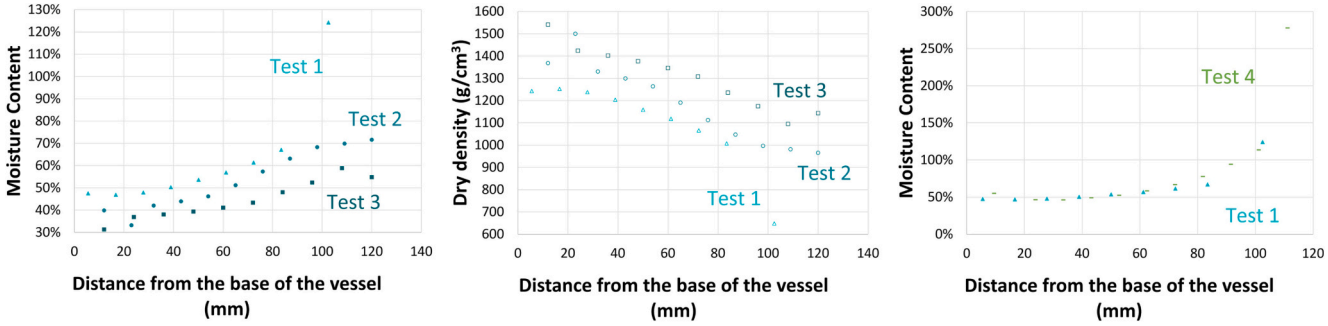

Fig. 6. Left and centre: The moisture content (left) and dry density (centre) profiles along the post-test samples for the 1 M NaCl Tests 1 (65 mm), 2 (75 mm) and 3 (85 mm), with linear fits. Right: Moisture content profiles for the 65 mm 1 M NaCl tests with different bentonites (Test 1: Na bentonite, and Test 4: Ca bentonite), best fit by third order polynomials.

also observed, with longer starting lengths corresponding to smaller overall moisture content increases throughout the sample length.

For Tests 2 and 3, both the moisture content and dry density data appeared to follow linear trends; the data from Test 1 however did not show the same trend. This sample, which had the shortest starting length (65 mm, Test 1), showed a much higher moisture content (>120%) and lower dry density (< 0.7 g/cm^3) for the first point of measurement (100 mm from the base of the sample) than any of the other measured pieces of clay, and this skewed a linear trend. This sample also showed higher moisture contents and lower dry densities for the last 2–3 points of measurement at the base of the sample than a linear fit would have suggested; the same was indicated in the last point of measurement at the base of the sample in Test 2. As the sample had free access to water at both its upper and lower surfaces, it was expected that the imbibition of water and swelling of the sample would have taken place at both ends. It was more unexpected that this was not apparent in the Test 3 data, which consistently followed a linear trend to the base of the vessel in both the moisture content and dry density data.

4. Discussion

The principle motivation of this study was to investigate the control of fluid salinity on the development of swelling pressure in bentonite whilst the material was expanding to fill a void space. The experiments have shown that bentonite can swell into and fully occupy a void space with an axial strain of up to 80%. However, the salinity of the test permeant, the bentonite composition and the axial strain experienced by the sample all controlled the size of the swelling pressure that the bentonite placed on the surrounding apparatus, as well as the strength of the material in the area of the apparatus that was originally void space at the start of the test.

Two closely-related previous studies have investigated the impact of an engineering void on the swelling pressure development in Wyoming-type Na bentonite under non-saline conditions at ambient [Harrington et al., 2020] and elevated [Daniels et al., 2021b] temperature conditions. At ambient temperature conditions, 3 tests were conducted (hereafter referred to as Tests D1-D3) with starting sample lengths of 65 mm, 75 mm and 85 mm respectively [Harrington et al., 2020]. Under elevated temperature conditions, 4 tests were conducted (hereafter referred to as tests T1-T4). Three of these were run at 90 °C and had starting sample lengths of 65 mm, 75 mm and 85 mm. The final test had a starting length of 95 mm and was conducted at 100 °C. Each of these tests was conducted using identical testing protocols and in either the same Daniels et al. [2021b] or similar Harrington et al. [2020] experimental apparatus to that used in this study. These previous studies have shown that the size of the voidage does impact upon the swelling pressure that develops in the bentonite over the 100 day testing duration [Harrington et al., 2020; Daniels et al., 2021a, b].

As is the case for the previous studies, the size of the void selected in these experiments was large in relation to the initial sample size, leading to a large axial swelling strain. For the largest voids the result gave, therefore, the behaviour under conditions approaching the limit of what might realisically occur in a repository. However, this provided us with an end member in order to delineate the form of the relationship under investigation. Before considering further the influence of strain on homogenisation of swelling pressure and the impact of a saline test permeant compared with deionised water, it is helpful to first highlight some of the commonalities observed for the 5 tests presented in this study.

A comparison of the swelling pressure development measured during this study (1 M NaCl test permeant; Fig. 7 A-C) was made, with a set of tests run under the same conditions except for the salinity of the test permeant (zero salinity case Harrington et al., 2020; Fig. 7 D—F). In all of the tests compared, peak pressures were measured on those axial and radial load cells closest to the base of the vessel. The peak values were all between 3 and 4 MPa. The swelling pressures measured on all sensors decreased asymptotically during the test, but inspection of the swelling pressure curves for the elevated salinity tests alongside their zero salinity counterparts highlighted that the degree of spread in swelling

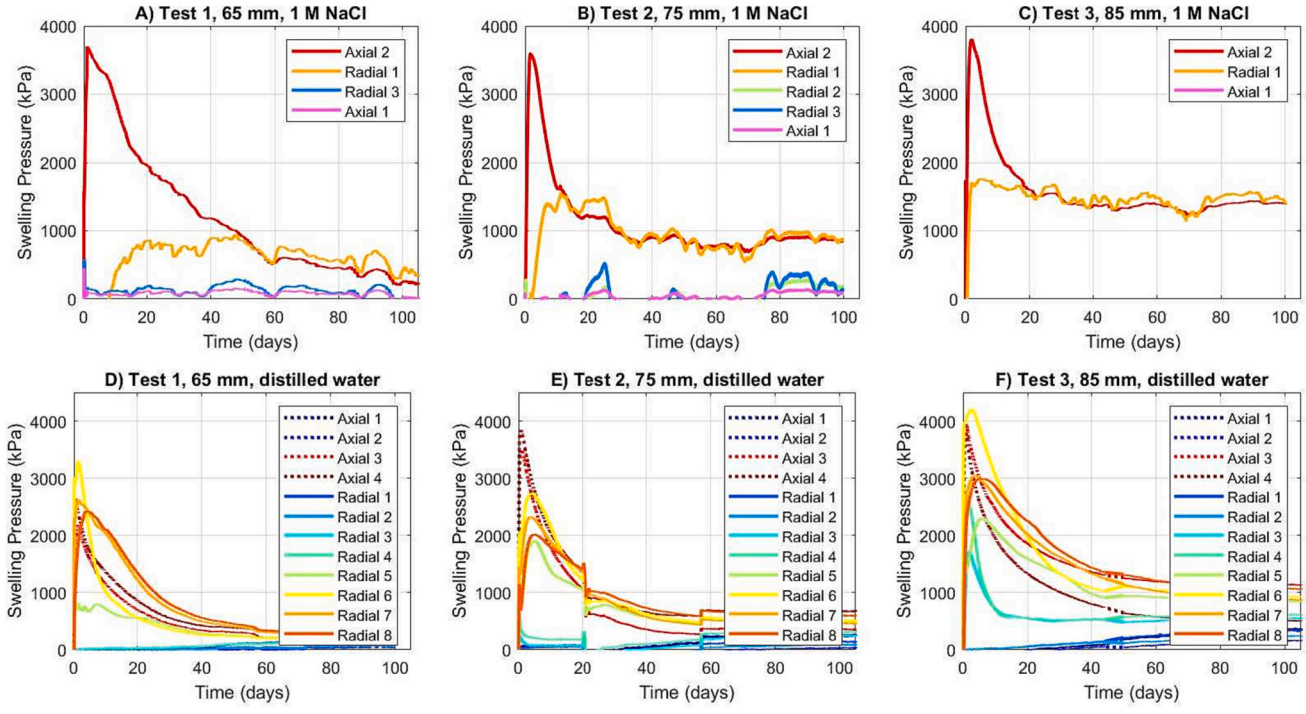

Fig. 7. Swelling pressure evolution for sample lengths of 65, 75 and 85 mm (left to right) at A)-C) elevated salinity conditions of 1 M NaCl (Tests 1–3 from this study), and D)-F) non-saline conditions using deionised water as the test permeant (Tests D1-D3 from Harrington et al., 2020). All of the tests were conducted at ambient temperatures, the same applied water pressure (4500 kPa), and the samples had dry densities of 1.7 g/cm^3. Each of the samples was manufactured from Wyoming-type MX80 bentonite.

pressures differed notably between experiments. A correlation between the degree of homogenisation and a larger initial void size (higher axial strain) was also clearly apparent. This behaviour can be explained by a comparatively greater drop in dry density resulting from the greater degree of expansion of the clay. A larger increase in hydraulic conductivity would have been expected to occur at these higher strains as the density of bentonite reduces, providing more rapid access to water along the sample length.

The pore pressure evolution showed a consistent behaviour across the 5 tests (Fig. 4, and Figures SM5 to SM9 in the supplementary material). In all tests, the pore pressure response was seen by the top array of sensors (PTs 1–4) first, followed by the central array (halfway down the length of the vessel, PTs 5 and 10–12); the bottom array of pore pressure sensors was the last to see a change in the pore pressure. In some tests, the pore pressure filters in the topmost array were not covered by the pre-test sample and thus the pore pressure measurement increased almost simultaneously with the applied water pressure increase at the start of the test. For the 65 mm samples, the top of the pre-test sample was 7 mm above the central pore pressure array, whilst the bottom array of sensors (PTs 13–16) was 36.6 mm from the applied water at the base of the sample. For the 85 mm sample, the top of the pre-test sample was 5.6 mm above the topmost array of pore pressure transducers and 27 mm above the central array. The distance between the top of the 85 mm pre-test sample and the central array of sensors was only 9.6 mm closer than the base of the sample to the bottom array of sensors (36.6 mm). It was not clear however, why the pore pressure increase at the bottom array of sensors in Test 3 (85 mm) took more than three times as long to be seen (days 28 to 38) as it did at the central array (days 5 to 10). One possible explanation lies in the fact that the top surface of the sample could expand upwards into the void space. Although the base of the sample had the same availability of fluid as the top, the sample was volumetrically constrained at the base. The effective dry density was able to evolve at the top surface, decreasing as the sample expanded upwards. This also progressively increased the permeability at the top end of the sample. The different response times of the individual pore pressure transducers in the same array however suggested that the migration of the water through the sample cannot be seen as a being one-dimensional along the sample axis. Instead, the water migration through the sample should be thought of as a locally three-dimensional process. The pore pressure observations were also consistent with the swelling pressures because they showed that hydraulic equilibrium was established more rapidly at higher axial swelling strains. The tests with 65 mm pre-test sample lengths saw an increase in pore pressure to 4500 kPa (the applied water pressure) at all of the sensors most quickly.

Pore pressure data was not recorded in the zero salinity tests of Harrington et al. [2020], so a direct comparison of the rate of migration of water through the sample between the saline and non-saline tests was not possible. However, the zero salinity elevated temperature tests presented by Daniels et al. [2021b] did record average pore pressure data in three arrays along the length of the testing apparatus, in an identical configuration to the tests presented here (please see Figures SM10 to SM12 in the supplementary material for a comparison of these data). The pore water ingress occurred more rapidly under saline conditions than under zero salinity and elevated temperature (90 °C) conditions, but it should be recognised that it was difficult to deconvolve the contribution of temperature from the test data. In addition, the swelling pressure data showed that the elevated salinity conditions limited the swelling process, and thus the interface between the sample and vessel wall may have been more permeable in the elevated salinity tests, acting as a conduit for fluid for longer at the start of the test period. This may also explain why the increase in pore pressure was seen much sooner on the central array than it was on the bottom array where the fluid had to pass most clay to reach the filters and sensors.

The swelling pressures have shown that after approximately the first 20 days, there was very little alteration in the magnitude of the measured values, and evolution of the system was very slow. Harjupatana et al. [2015] and Harjupatana et al. [2022] have used X-Ray tomography and tracer particles to show that at a bentonite-water contact, a narrow zone of markedly increased water content can rapidly form, which simultaneously causes local swelling of the bentonite and compaction elsewhere in the sample. Whilst their samples were only imaged for the first 4 days of testing, were a significantly smaller size and used water as the test fluid, they also showed that the progress of the fluid into the sample may not have been linear across the sample. This immediate formation of a wet zone close to the fluid inlet point is also supported by the observations of Krohn [2004] who reported a decompressed region adjacent to the fluid inlet which uptook more water than the theoretical maximum (31%) and for which the water content was not dependent on the test duration. Both of these test programmes were conducted under ambient pressure conditions, but support the possiblity that a zone of increased water content formed at the base of the sample early in the test history. The sensor spacing was too sparse to allow a narrow wet zone at the sample base to be detected, but the moisture content measurements from the base of the vessel showed some indication of a slight increase in the sample slice immediately adjacent to the base of the vessel (Fig. 6 and Figure SM13 in the supplementary material).

Where the data were available in the elevated salinity tests, on the axial and radial load cells closest to the top of the test apparatus negative swelling pressures were calculated. The water pressure was applied to each end of the sample at the start of the test period; the assumption made during testing was that when the water pressure was applied, it was felt instantaneously and uniformly across the apparatus. Thus the calculation of the swelling pressure arose from the subtraction of the average applied water pressure from the total stress. For the sensors sited adjacent to the clay, provided the applied water had permeated into the clay, the clay should have exerted a force over and above the applied water pressure on the load cell. This was clearly the case for the axial load cell at the base of the vessel, where there was both clay and fluid availability. For the radial load cells sited next to the clay, initially there was no fluid availability so the clay could not swell, and therefore the swelling pressure started as −4500 kPa and gradually increased as fluid availability increased. The negative values reported at early times in the test history indicated that there was disequilibrium existing in the system until the fluid penetrated the clay. For the load cells sited next to the void space, the total stress should have equalled the applied water pressure, since there was no clay adjacent to the sensor to provide an additional component of swelling pressure. This was the case in Tests 1 and 2 (1 M NaCl, 65 and 75 mm samples), but in the other tests, the calculated swelling pressures were consistently below zero. Since the stress sensors were also still reporting positive values under the testing conditions, it was reasonable to conclude that these values were real.

The swelling pressure curves of the tests presented in this study also notably showed more variability than in their zero salinity counterparts, especially (where recorded) on the radial sensor R3 (Fig. 7B), which was closest to the top of the apparatus. The swelling pressure data from the base of the apparatus were significantly less variable, and were much more comparable with the smooth swelling pressure curves recorded in the zero salinity tests [Harrington et al., 2020]. It was possible that the variability in swelling pressure recorded represented an intermittent and piecewise expansion of the sample, which may have been caused by friction between the sample and the side walls of the apparatus. Additional testing using a repeated lead shot arrangement will allow the degree and scaling of such effects to be quantified and used to validate the handling of frictional effects in numerical models. However, it is important to note that the type of sensor used in the two tests was different; the zero salinity tests used a sensor behind a membrane that touched on the surface of the clay, whilst the elevated salinity tests used a button load cell with a pushrod that could be prone to hysteresis. It was therefore not surprising that the zero salinity swelling pressure data

were smoother.

To compare swelling pressure development between tests, the average swelling pressures were calculated over an interval of 30 data points at day 100 of each experiment, roughly equivalent to the final 6 h of data. At the end of each test, there was still often a large difference in the measured stresses between each sensor (Fig. 8). The zero salinity tests [Harrington et al., 2020] allowed a significantly larger number of stress measurements to be made (2 axial in each end closure (4 total) and 8 radial). Whilst the same level of interrogation was not possible with the smaller number of sensors available in the elevated salinity tests presented here, a crude approximation of the degree of heterogeneity in the clay was given by comparing the averaged axial swelling pressure value at each end of the vessel against the other, at the end of the test period. The average swelling pressure values were found to be substantially lower for the axial sensor closest to the top of the pressure vessel than for the sensor closest to the base.

Comparing the average axial swelling pressures as a function of axial strain for Tests 1–3 of this study with their zero salinity equivalent (Tests D1-D3 Harrington et al., 2020) (Fig. 8), the difference in swelling pressures at the top and base was clearly apparent, with the base of the samples giving a much larger final averaged axial swelling pressure measurement. This was consistent with the density gradient in the sample, which persisted up to 100 days. At the base of the sample, a general trend of decreasing final averaged axial swelling pressure at higher axial strains was also clear. This behaviour can be explained by the greater reduction in average sample density as a consequence of the swelling necessary to fill the void space. At the top of the vessel, for zero salinity conditions, the trend for decreasing swelling pressure with increasing axial strain remained true. However, under the elevated salinity conditions, swelling pressure was essentially absent at the top of the sample. The top end of the lowest axial strain test in the elevated salinity case showed a final averaged axial swelling pressure that was even lower than the general trend (Fig. 8), and this point plotting much higher on the y-axis would have been expected to align with the consistent negative correlation of final averaged axial swelling pressure with axial strain. Irrespective of the test conditions, for decreasing axial strains the swelling pressure was expected to increase simply because there was more clay material present inside the apparatus (i.e. the average dry density of the post-test sample was higher).

Looking further at the average axial swelling pressures (Fig. 8), those measured at the base (high density end) of the sample under elevated salinities were greater than those measured in the tests using deionised water (zero salinity case) for the two of the three tests compared with the lower axial strains (longer pre-test sample lengths). The pre-test sample lengths (and therefore mass of clay in the system) were the same in both sets of experiments (saline vs non-saline). These final swelling pressures tied in with the post-test moisture contents (Figure SM13), and showed that higher clay dry densities have persisted longer in the original location of the clay sample under elevated salinity conditions. The average axial swelling pressures measured at the top of the apparatus were uniformly higher in the zero salinity case. The greater swelling pressure difference reported across the whole sample (base minus top) in the elevated salinity case indicated that the bentonite experienced a reduced ability to homogenise in the presence of a saline permeant. Because very little alteration in the swelling pressures were seen after the first few days of testing (post-peak swelling pressure), this heterogeneity in the clay may be essentially locked in. These findings suggested that the suppression of clay swelling at higher salinities was likely to strongly impact the void-filling process. The rate of pressure change observed during the latter stages of testing was very small in all tests, thus extrapolation of the results suggested that complete homogenisation of the bentonite would not occur for many years, if at all. However, it was clear that bentonite, under zero hydraulic gradient and elevated salinity conditions, was able to swell and ultimately fill the start void, creating a small but measurable swelling pressure in the axial sensors above the sample (where a void was initially present) in all but the 3 M NaCl case (Test 5).

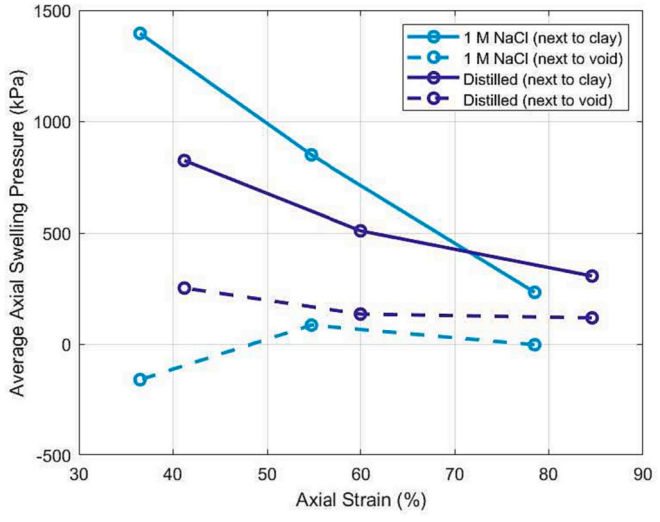

Fig. 8. Average axial swelling pressure after 100 days, as a function of axial strain resulting from swelling, comparing the elevated salinity tests presented here (Tests 1, 2 and 3) with their zero salinity [Harrington et al., 2020] counterparts.

The post-test moisture content and corresponding dry density profiles were much flatter in the elevated salinity tests presented in this study (particularly Tests 2 and 3) and showed a much more linear change in the moisture content along the sample length (Fig. 6, and Figure SM13 in the supplementary material). Due to the mass of salt added to these experiments via the test permeant, the calculation of the moisture content will have been very slightly underestimated and the dry density overestimated unless the salt mass was corrected for. In these experiments, the salt mass added ranged between approximately 5 and 8 g (Tests 1–4). The mass of salt added to Test 5 was higher reflecting the stronger concentration test permeant, however post-test moisture contents were not obtained for this test. The small fraction of salt mass made only a very small difference to the calculated dry densities, and as the sample was saturated with deionised water prior to being placed in the apparatus and the distribution of the salt within the post-test sample was unknown, a correction for salt mass fraction was not applied to the moisture content data. In the zero salinity case, significant swelling was seen within the upper 45–55 mm of each post-test sample; in this region a three-fold increase in moisture contents was recorded (please see Fig. 10 in Harrington et al., 2020). In the elevated salinity Tests 1 and 4 (65 mm sample), the moisture content profiles were very similar to the zero salinity case, with a large increase in the moisture content seen over a similar section at the top of the sample (top 45–55 mm of the samples) (please see Figure SM13 in the supplementary material). This suggested that despite the differences in the magnitude of the generated swelling pressures caused by the saline conditions, the test fluid was able to permeate into the sample at a similar rate.

However, in contrast to this, in the elevated salinity Tests 2 and 3, the moisture content values were unexpectedly uniform throughout the sample length; over the upper 45–55 mm of each sample there was no large increase in the moisture content. Some of the zero-salinity samples also showed very slightly higher moisture contents at the base of the sample, adjacent to the filter in the end closure of the apparatus, through which the water pressure was applied. This slightly higher moisture content at the base of the sample was present but reduced in Test 2 and absent in the data from Test 3, which could indicate that the test permeant was able to penetrate the sample less easily under elevated salinity conditions. Why this would be the case is unclear, but it is consistent with the possible existence of a higher permeability pathway at the sides of the sample (an experimental artefact and consequence of

the requirement to slot the sample into the experimental apparatus) for a longer period at the start of each test whilst the sample was swelling within the apparatus; it may also have reflected the suppression of the swelling response of the clay by the elevated salinity conditions, or could have represented differences in the evolution of the bentonite in the region immediately adjacent to the base of the test vessel, where the bentonite was confined but with free access to the wetting fluid.

5. Conclusions

A suite of 5 experiments were conducted examining the role of NaCl salinity and bentonite clay composition in the evolution of swelling and pore pressure development as a function of the degree of swelling permitted into a void space. Some key observations were made; firstly in almost all tests (with Test 5, 3 M NaCl being the exception), after 100 days the clay had fully swelled into the void and differential swelling pressures had reduced substantially. This emphasised the enormous capacity of bentonite to fill a void, even in more extreme scenarios. In almost all the tests however, differential pressures across the sample length were still significant at the end of testing (day 100), despite the overall rate of pressure decline having reduced to low levels at this time. Secondly, the larger the axial strain experienced by the material, the smaller the swelling pressures that were measured along the sample length, as might be expected by the reduction in dry density reducing swelling capacity. For the experiments at elevated salinity however, the clay at the top of the vessel never generated significant swelling pressures during the testing period. Thirdly, both the salinity and the bentonite composition influenced the rate of pore pressure evolution. The Ca bentonite (Test 4) demonstrated a faster pore pressure evolution than the Na bentonite under the same conditions. Pore pressure evolution in all tests was seen to occur in a staggered fashion along the length of the vessel, with hydraulic equilibrium apparently being reached more rapidly under higher salinity conditions. This was likely to be due to the reduced swelling ability of the clay caused by the elevated salinity, leading to the persistence of more permeable fluid pathways at the edges of the sample for longer at the beginning of the test period. In general however, for a given salinity the time period required for apparent hydraulic equilibrium to be reached along the sample length was shortest for those samples that experienced the greatest degree of axial strain. This was consistent with the observations in relation to residual heterogeneity, which was found to be highest for those samples that experienced the smallest axial swelling strains.

The primary implication of these tests is that the larger the space available for free swelling present, the greater the capacity for the clay to reach hydraulic equilibrium and thus the faster the homogenisation of swelling pressures. In addition, whilst it was seen that for higher salinities the pore pressures appeared to equilibrate faster, this did not correspond to an ability of the clay to generate a swelling pressure at the far end of the experimental apparatus. Further work using this dataset should help to assess the rate at which swelling pressure homogenisation occurs as a function of strain. This will provide a better understanding of likely swelling pressure ranges that may be expected both at lower strains and under elevated salinities, such as those that might be expected near evaporite formations. Such information is key to assessing whether any residual heterogeneity is significant or can be tolerated. Further testing and method development of the XCT for this application will allow stronger conclusions to be made on the distribution of swelling along the sample. In addition, analysis of the expected hydraulic conductivity and swelling pressure at equilibrium conditions and in a high salinity environment without swelling would provide a useful contribution to our understand of the impact of salinity. The data generated by these experiments also provide a suitable resource for parameterisation and validation of numerical models that can further assess the long-term homogenisation behaviour of bentonite in geological disposal facilities.

Credit author statement

Katherine Daniels: Methodology, Formal Analysis, Investigation, Writing – Original Draft, Visualization, Project Administration. **Caroline Graham:** Formal Analysis, Investigation, Writing - Review & Editing, Project Administration, Funding Acquisition. **Andrew Wiseall:** Investigation, Writing - Original Draft. **Jon Harrington:** Conceptualization, Methodology, Investigation, Writing - Review & Editing, Supervision, Funding Acquisition. **Patrik Sellin:** Conceptualization, Resources.

Declaration of Competing Interest

The authors declare that they have no known competing financial interests or personal relationships that could have appeared to influence the work reported in this paper.

Data availability

Data will be made available on request.

Acknowledgements

This research was funded by the European Commission Bentonite Mechanical Evolution (BEACON) project, with grant number 745942. This work was also supported by the Institute for Korea Spent Nuclear Fuel (iKSNF) and National Research Foundation of Korea (NRF) grant funded by the Korea government (Ministry of Science and ICT, MSIT) (2021M2E1A1085193). Svensk Karnbranslehantering AB (SKB) and Korea Atomic Energy Research Institute (KAERI) provided the Na and Ca bentonite powders respectively. The authors acknowledge Dr. Elena Tamayo-Mas of the British Geological Survey for reviewing an earlier version of the manuscript. Simon Holyoake is thanked for his assistance with the experimental apparatus instrumentation and data acquisition. Humphrey Wallis and Wayne Leman are also thanked for their help in the design and manufacture of the experimental apparatus and the careful preparation of the test samples. Finally, we wish to thank the Core Scanning Facility (CSF) at the British Geological Survey (BGS) for providing access to the CT core scanner and their technical support and expertise. The samples used herein were specifically manufactured for the test programme using supplied powders; they were destructively tested during the study, providing the information on post-test moisture content. The authors declare no conflict of interest. The funders had no role in the design of the study; in the collection, analyses, or interpretation of data; in the writing of the manuscript, or in the decision to publish the results. This paper is published with the permission of the Director of the British Geological Survey part of United Kingdom Research and Innovation (UKRI).

Appendix A. Supplementary data

Supplementary data to this article can be found online at https://doi.org/10.1016/j.clay.2023.107200.

References

Andra, 2005. Référentiel des matériaux d'un stockage de déchets à haute activité et à vie longue—Tome 4: Les matériaux à base d'argilites excavées et remaniées. Technical Report, France.

Bian, X., Cui, Y.J., Li, X.Z., 2018. Voids effect on the swelling behaviour of compacted bentonite. Géotechnique 17, 283. https://doi.org/10.1680/jgeot.17.p.283.

Börgesson, L., Pusch, R., 1987. Rheological Properties of a Calcium Smectite. Technical Report, Stockholm, Sweden.

Brackley, I.J.A., 1973. Swe`ll pressure and free swell in a compacted clay. In: Proceedings of the 3rd International Conference on Expansive Soils. Haifa, pp. 169–176.

Bradbury, M.H., Baeyens, B., 2003. Porewater chemistry in compacted re-saturated MX-80 bentonite. J. Contam. Hydrol. 61, 329–338.

Brady, P.V., Kozak, M.W., 1995. Geochemical engineering of low level radioactive waste in cementitious environments. Waste Manag. 15, 293–301. https://doi.org/10.1016/0956-053X(95)00028-X.
Caballero, E., Jimenez de Cisneros, C., Linares, J., 2004. Physicochemical properties of bentonite: effect of the exchangeable cations. In: FEBEX II Project. THG laboratory experiments (T. Missana, editor). Technical Report. Madrid, Spain.
Castellanos, E., Villar, M.V., Romero, E., Lloret, A., Gens, A., 2008. Chemical impact on the hydro-mechanical behaviour of highdensity FEBEX bentonite. Phys. Chem. Earth 33, S516–S526. https://doi.org/10.1016/j.pce.2008.10.056.
Chapman, N., 2006. Geological disposal of radioactive wastes. J. Iber. Geol. 32, 7–14.
Chapman, N., Hooper, A., 2012. The disposal of radioactive wastes underground. Proceedings of the Geol. Assoc. 123, 46–63.
Chen, W.C., Huang, W.H., 2013. Effect of groundwater chemistry on the swelling behavior of a Ca-bentonite for deep geological repository. Phys. Chem. Earth 65, 42–49. https://doi.org/10.1016/j.pce.2013.05.012.
Chen, Y.G., Zhu, C.M., Ye, W.M., Cui, Y.J., Wang, Q., 2015. Swelling pressure and hydraulic conductivity of compacted GMZ01 bentonite under salinization-desalinization cycle conditions. Appl. Clay Sci. 114, 454–460. https://doi.org/10.1016/j.clay.2015.06.033.
Chen, Y.G., Zhu, C.M., Ye, W.M., Cui, Y.J., Chen, B., 2016. Effects of solution concentration and vertical stress on the swelling behavior of compacted GMZ01 bentonite. Appl. Clay Sci. 124-125, 11–20. https://doi.org/10.1016/j.clay.2016.01.050.
Chen, Y.G., Dong, X.X., Zhang, X.D., Ye, W.M., Cui, Y.J., 2018. Combined thermal and saline effects on the swelling pressure of densely compacted GMZ bentonite. Appl. Clay Sci. 166, 318–326. https://doi.org/10.1016/j.clay.2018.10.001.
Chen, Y.G., Cai, Y.Q., Ye, W.M., Wang, Q., 2022. Influence of dry density and water salinity on the swelling pressure and hydraulic conductivity of compacted GMZ01 bentonite–sand mixtures. Acta Geotech. 17, 1879–1896. https://doi.org/10.1007/s11440-021-01305-7.
Chun-Ming, Z., Ye, W.M., Chen, Y.G., Chen, B., Cui, Y.J., 2013. Influence of salt solutions on the swelling pressure and hydraulic conductivity of compacted GMZ01 bentonite. Eng. Geol. 166, 74–80. https://doi.org/10.1016/j.enggeo.2013.09.001.
Coulon, H., 1987. Proprietes physico-chimiques des sediments argileux francais: Application au stockage des dechets radioactifs. Thesis. University of Lille, France.
Coulon, H., Lajudie, A., Debrabant, P., Atabek, R., Jordia, M., Jehan, R.A., 1987. Choice of French clays as engineered barrier components for waste disposal. Sci. Basis Nucl. Waste Manag. 10, 813–824. https://doi.org/10.1557/PROC-84-813.
Cui, Y.J., 2017. On the hydro-mechanical behaviour of MX80 bentonite-based materials. J. Rock Mech. Geotech. Eng. 9, 565–574. https://doi.org/10.1016/j.jrmge.2016.09.003.
Daniels, K.A., Harrington, J.F., Jensen, M., 2017. Permeability measurements from a potential deep geological repository site. In: International High-Level Radioactive Waste Management Conference 16th International High Level Radioactive Waste Management Conference (IHLRWM 2017) Proceedings.
Daniels, K.A., Harrington, J.F., Milodowski, A.E., Kemp, S.J., Mounteney, I., Sellin, P., 2021a. Gel Formation at the Front of Expanding Calcium Bentonites. Minerals 11, 215. https://doi.org/10.3390/min11020215.
Daniels, K.A., Harrington, J.F., Sellin, P., Norris, S., 2021b. Closing repository void spaces using bentonite: does heat make a difference? Appl. Clay Sci. 210, 106124.
Delage, P., Cui, Y.J., Tang, A., 2010. Clays in radioactive waste disposal. J. Rock Mech. Geotech. Eng. 2, 111–123.
Di Maio, C., 1996. Exposure of bentonite to salt solution: osmotic and mechanical effects. Géotechnique 46, 695–707.
Dontsova, K.M., Norton, L.D., Johnston, C.T., Bigham, J., 2004. Influence of exchangeable cations on water adsorption by soil clays. Soil Sci. Soc. Am. J. 68, 1218–1227.
Dueck, A., Goudarzi, R., Börgesson, L., 2016. Buffer Homogenisation: Status Report 3. Technical Report, Stockholm, Sweden.
Dueck, A., Börgesson, L., Kristensson, O., Malmberg, D., Åkesson, M., Hernelind, J., 2019. Bentonite Homogenisation: Laboratory Study, Model Development and Modelling of Homogenisation Processes. Technical Report, Stockholm, Sweden.
Gens, A., Valleján, B., Sánchez, M., Imbert, C., Villar, M.V., Van Geet, M., 2011. Hydromechanical behaviour of a heterogeneous compacted soil: experimental observations and modelling. Géotechnique 61, 367–386. https://doi.org/10.1680/geot.SIP11.P.015.
Goo, J.Y., Kim, B.J., Kwon, J.S., Jo, H.Y., 2023. Bentonite alteration and retention of cesium and iodide ions by Ca-bentonite in alkaline and saline solutions. Appl. Clay Sci. 245, 107141 https://doi.org/10.1016/j.clay.2023.107141.
Hall, P.L., Astill, D.M., 1989. Adsorption of water by homoionic exchange forms of Wyoming montmorillonite (SWy-1). Clay Clay Miner. 37, 355–363. https://doi.org/10.1346/CCMN.1989.0370409.
Harjupatana, T., Alaraudanjoki, J., Kataja, M., 2015. X-ray tomographic method for measuring three-dimensional deformation and water content distribution in swelling clays. Appl. Clay Sci. 114, 386–394. https://doi.org/10.1016/j.clay.2015.06.016.
Harjupatana, T., Miettinen, A., Kataja, M., 2022. A method for measuring wetting and swelling of bentonite using X-ray imaging. Appl. Clay Sci. 221, 106485 https://doi.org/10.1016/j.clay.2022.106485.
Harrington, J.F., Tamayo-Mas, E., 2016. Observational Evidence for the Differential Development of Porewater Pressure within Compact Bentonite and its Impact on Permeability and Swelling Pressure. Technical Report, Nottingham, UK.
Harrington, J.F., Daniels, K.A., Tamayo-Mas, E., 2017. Homogenisation on the Laboratory Scale: Development of Porewater Pressure and Stress in Bentonite. Technical Report, Nottingham, UK.
Harrington, J.F., Daniels, K.A., Wiseall, A.C., Sellin, P., 2020. Bentonite homogenisation during the closure of void spaces. Int. J. Rock Mech. Min. Sci. 136, 104535 https://doi.org/10.1016/j.ijrmms.2020.104535.
He, Y., Ye, W.M., Chen, Y.G., Ye, B., Cui, Y.J., 2016. Influence of pore fluid concentration on water retention properties of compacted GMZ01 bentonite. Appl. Clay Sci. 129, 131–141. https://doi.org/10.1016/j.clay.2016.05.020.
Hella, P., Pitkanen, P., Lofman, J., Partamies, S., Vuorinen, U., Wersin, P., 2010. Safety Case for the Disposal of Spent Nuclear Fuel at Olkiluoto. Technical Report. Eurajoki, Finland, Definition of Reference and Bounding Groundwaters, Buffer and Backfill Porewaters.
Herbert, H., Kasbohm, J., Sprenger, H., Fernández, A., Christian, R., 2008. Swelling pressures of MX-80 bentonite in solutions of different ionic strength. Phys. Chem. Earth 33, S327–S342.
Idiart, A., Pekala, M., 2016. Models for Diffusion in Compacted Bentonite. Technical Report, Stockholm, Sweden.
Imbert, C., Villar, M.V., 2006. Hydro-mechanical response of a bentonite pellets/powder mixture upon infiltration. Appl. Clay Sci. 32, 197–209. https://doi.org/10.1016/j.clay.2006.01.005.
International Atomic Energy Agency, 2003. Scientific and Technical Basis for the Geological Disposal of Radioactive Wastes. Technical Report, New York.
Jia, L.Y., Chen, Y.G., Ye, W.M., Cui, Y.J., 2019. Effects of a simulated gap on anisotropic swelling pressure of compacted GMZ bentonite. Eng. Geol. 248, 155–163. https://doi.org/10.1016/j.enggeo.2018.11.018.
Juvankoski, M., 2010. Description of Basic Design for Buffer. Technical Report, Eurajoki, Finland.
Karnland, O., 1997. Bentonite Swelling Pressure in Strong NaCl Solutions. Correlation between model calculations and experimentally determined data. Technical Report, Stockholm, Sweden.
Karnland, O., Muurinen, A., 2002. Bentonite swelling pressure in NaCl solutions - experimentally determined data and model calculations. In: Clays In Natural And Engineered Barriers For Radioactive Waste Confinement, International Meeting, pp. 175–176.
Karnland, O., Muurinen, A., Karlsson, F., 2005. Bentonite swelling pressure in NaCl solutions - Experimentally determined data and model calculations. In: Advances in Understanding Engineered Clay Barriers - Proceedings of the International Symposium on Large Scale Field Tests in Granite, pp. 241–256.
Karnland, O., Olsson, S., Nilsson, U., 2006. Mineralogy and Sealing Properties of Various Bentonites and Smectite-Rich Clay Materials. Technical Report, Stockholm, Sweden.
Komine, H., 2010. Predicting hydraulic conductivity of sand bentonite mixture backfill before and after swelling deformation for underground disposal of radioactive wastes. Eng. Geol. 114, 123–134.
Komine, H., Yasuhara, K., Murakami, S., 2009. Swelling characteristics of bentonites in artificial seawater. Can. Geotech. J. 46, 177–189.
Krohn, K.P., 2004. Proposal of an alternative re-saturation model for bentonite buffers — the conceptual model, the numerical model and the data base. Proceedings from Task Force-related Meeting on Buffer and Backfill Modelling 95–101.
Li, Z., Su, G., Zheng, Q., Nguyen, T.S., 2020. A dual-porosity model for the study of chemical effects on the swelling behaviour of MX-80 bentonite. Acta Geotech. 15, 635–653. https://doi.org/10.1007/s11440-019-00762-5.
Linares, J., 1989. Spanish Research Activities in Thefield of Backfilling and Sealing: A Pre-Liminary Study of some Spanish Sedimentary (Madrid Basin) and Hydrothermal (Almeria) Bentonite. Technical Report, Paris.
Liu, L., 2010. Permeability and expansibility of sodium bentonite in dilute solutions. Colloids Surf. A Physicochem. Eng. Asp. 358, 68–78. https://doi.org/10.1016/j.colsurfa.2010.01.033.
Liu, L., 2013. Prediction of swelling pressures of different types of bentonite in dilute solutions. Colloids Surf. A Physicochem. Eng. Asp. 434, 303–318. https://doi.org/10.1016/j.colsurfa.2013.05.068.
Ltd., I.E., 2011. OPG's Deep Geological Repository for Low and Intermediate Level Waste. Descriptive Geosphere Site Model. Technical Report, Canada.
Marcial, D., Delage, P., Cui, Y.J., 2002. On the high stress compression of bentonites. Can. Geotech. J. 39, 812–820. https://doi.org/10.1139/t02-019.
Martin, P.L., Barcala, J.M., Huertas, F., 2006. Large-scale and long-term coupled thermo-hydro-mechanic experiments with bentonite: the febex mock-up test. J. Iber. Geol. 32, 259–282.
Massat, L., Cuisinier, O., Bihannic, I., Claret, F., Pelletier, M., Masrouri, F., Gaboreau, S., 2016. Swelling pressure development and inter-aggregate porosity evolution upon hydration of a compacted swelling clay. Appl. Clay Sci. 124-125, 197–210.
Mata, C., 2003. Hydraulic Behaviour of Bentonite Based Mixtures in Engineered Barriers: The Backfill and Plug Test at the Äspö HRL (Sweden). Technical University of Catalonia (PhD Thesis).
NAGRA, 1985. Project Gewahr 1985, Nuclear Waste Management in Switzerland: Feasibility Studies and Safety Analysis (Technical Report).
Navarro, V., De la Morena, G., Yustres, A., Gonzalex-Arteaga, J., Asensio, L., 2017a. Predicting the swelling pressure of MX-80 bentonite. Appl. Clay Sci. 49, 51–58. https://doi.org/10.1016/j.clay.2017.08.014.
Navarro, V., Yustres, A., Asensio, L., De la Morena, G., Gonzalex-Arteaga, J., Laurila, T., Pintado, X., 2017b. Modelling of compacted bentonite swelling accounting for salinity effects. Eng. Geol. 223, 48–58. https://doi.org/10.1016/j.enggeo.2017.04.016.
Pusch, R., 1977. Required Physical and Mechanical Properties of Buffer Masses. Technical Report, Stockholm, Sweden.
Pusch, R., 2001. The Microstructure of MX-80 Clay with Respect to its Bulk Physical Properties under Different Environmental Conditions. Technical Report, Stockholm, Sweden.

Rhén, I., Gustafson, G., Wikberg, P., 1997. Results from Pre-Investigations and Detailed Site Characterization. Hydrogeology, groundwater chemistry and transport of solutes. Technical Report. Stockholm, Sweden, Comparison of predictions and observations.
Sellin, P., Leupin, O.X., 2013. The use of clay as an engineered barrier in radioactive waste management—a review. Clay Clay Miner. 61, 477–498. https://doi.org/10.1346/CCMN.2013.0610601.
Siddiqua, S., Blatz, J., Siemens, G., 2011. Evaluation of the impact of pore fluid chemistry on the hydromechanical behaviour of clay-based sealing materials. Can. Geotech. J. 48, 199–213. https://doi.org/10.1139/T10-064.
SKB, 1983. Final Storage of Spent Nuclear Fuel—KBS-3. Technical Report, Stockholm, Sweden.
SKB, 2007. RD&D-Programme. Technical Report, Stockholm, Sweden.
SKB, 2011. Long-Term Safety for the Final Repository for Spent Nuclear Fuel at Forsmark: Main Report of the SR-Site Project, Volume 1. Technical Report, Stockholm, Sweden.
Stockdale, A., Bryan, N.D., 2013. The influence of natural organic matter on radionuclide mobility under conditions relevant to cementitious disposal of radioactive wastes: a review of direct evidence. Earth Sci. Rev. 121, 1–17. https://doi.org/10.1016/j.earscirev.2013.02.007.
Studds, P.G., Stewart, D.I., Cousens, T.W., 1998. The effects of salt solutions on the properties of bentonite–sand mixtures. Clay Miner. 33, 651–660.
Sun, D., Zhang, L., Li, J., Zhang, B., 2015. Evaluation and prediction of the swelling pressures of GMZ bentonites saturated with saline solution. Appl. Clay Sci. 105-106, 207–216. https://doi.org/10.1016/j.clay.2014.12.032.
Sun, H., Mašín, D., Boháč, J., 2017. Experimental characterization of retention properties and microstructure of the Czech bentonite B75. In: Proceedings of the 19th International Conference on Soil Mechanics and Geotechnical Engineering. Seoul, Korea.
Svemar, C., Johannesson, L.E., Grahm, P., Svensson, D., 2016. Prototype Repository: Opening and Retrieval of Outer Section of Prototype Repository at Äspö Hard Rock Laboratory. Technical Report, Stockholm, Sweden.
Svensson, D., Lundgren, C., Johannesson, L.E., Norrfors, K., 2017. Developing Strategies for Acquisition and Control of Bentonite for a High Level Radioactive Waste Repository. Technical Report, Stockholm, Sweden.
Svoboda, J., 2013. The experimental study of bentonite swelling into fissures. Clay Miner. 48, 383–389.
Tabak, A., Afsin, B., Caglar, B., Koksal, E., 2007. Characterization and pillaring of a Turkish bentonite (Resadiye). J. Colloid Interface Sci. 313, 5–11.
Tessier, D., Dardaine, M., Beaumont, A., Jaumet, A.M., 1998. Swelling pressure and microstructure of an activated swelling clay with temperature. Clay Miner. 33, 255–267. https://doi.org/10.1180/000985598545615.
Vieno, T., Hautojarvi, A., Koskinen, L., Nordman, H., 1992. TVO-92 Safety Analysis Ofspent Fuel Disposal. Technical Report, Finland.
Villar, M.V., 2002. Thermo-hydro-mechanical characterisation of a bentonite from Cabo de Gata. A study applied to the use of bentonite as sealing material in high level radioactive waste repositories. Technical Report, Madrid, Spain.
Villar, M.V., 2005. MX-80 Bentonite. Thermal–Hydro-Mechanical Characterisation Performed at CIEMAT in the Context of the Prototype Project. Technical Report, Madrid, Spain.
Villar, M.V., 2007. Water retention of two natural compacted bentonites. Clay Clay Miner. 55, 311–322. https://doi.org/10.1346/CCMN.2007.0550307.
Villar, M.V., Lloret, A., 2008. Influence of dry density and water content on the swelling of a compacted bentonite. Appl. Clay Sci. 39, 38–49. https://doi.org/10.1016/j.clay.2007.04.007.
Villar, M.V., Iglesias, R.J., García-Siñeriz, J.L., 2020. State of the in situ Febex test (GTS, Switzerland) after 18 years: a heterogeneous bentonite barrier. Environ. Geotech. 7, 147–159. https://doi.org/10.1680/jenge.17.00093.
Wang, Q., Tang, A.M., Cui, Y.J., Delage, P., Barnichon, J.D., Ye, W.M., 2013. The effects of technological voids on the hydro-mechanical behaviour of compacted bentonite–sand mixture. Soils Found. 53, 232–245. https://doi.org/10.1016/j.sandf.2013.02.004.
Wang, Q., Cui, Y.J., Tang, A.M., Delage, P., Gatmiri, B., Ye, W.M., 2014. Long-term effect of water chemistry on the swelling pressure of a bentonite-based material. Appl. Clay Sci. 87, 157–162. https://doi.org/10.1016/j.clay.2013.10.025.
Watanabe, Y., Yokoyama, S., 2021. Self-sealing behavior of compacted bentonite–sand mixtures containing technological voids. Geomech. Energ. Environ. 25, 100213 https://doi.org/10.1016/j.gete.2020.100213.
Wersin, P., Kiczka, M., Koskinen, K., 2016. Porewater chemistry in compacted bentonite: Application to the engineered buffer barrier at the Olkiluoto site. Appl. Geochem. 74, 165–175. https://doi.org/10.1016/j.apgeochem.2016.09.010.
Whitlow, R., 2004. Geotechnics 4 Checkbook. Butterworths and Co.
Wigger, C., Hanusova, I., Hausmannova, L., Heino, L., Lavikainen, V., Leupin, O.X., Marshall, P., Mayor, J.C., Meleshyn, A., Pusch, R., Sellin, P., Swahn, J., Talandier, J., Wendling, J., Wieczorek, K., 2017. Deliverable D1.1, State-of-the-Art Report, Beacon - Bentonite Mechanical Evolution. Technical Report. EC grant agreement No. 745942.
Ye, W.M., Cui, Y.J., Qian, L.X., Chen, B., 2009. An experimental study of the water transfer through confined compacted GMZ bentonite. Eng. Geol. 108, 169–176. https://doi.org/10.1016/j.enggeo.2009.08.003.
Zeng, Z.X., Cui, Y.J., Conil, N., Talandier, J., 2020. Experimental study on the aeolotropic swelling behaviour of compacted bentonite/claystone mixture with axial/radial technological voids. Eng. Geol. 278, 105846 https://doi.org/10.1016/j.enggeo.2020.105846.
Zhang, F., Ye, W.M., Wang, Q., Chen, Y.G., Chen, B., 2019. An insight into the swelling pressure of GMZ01 bentonite with consideration of salt solution effects. Eng. Geol. 251, 190–196. https://doi.org/10.1016/j.enggeo.2019.02.016.
Zhu, C.M., Ye, W.M., Chen, Y.G., Chen, B., Cui, Y.J., 2013. Influence of salt solutions on the swelling pressure and hydraulic conductivity of compacted GMZ01 bentonite. Eng. Geol. 166, 74–80. https://doi.org/10.1016/j.enggeo.2013.09.001.